Polymer 358 (2026) 130126

Contents lists available at ScienceDirect

Polymer

journal homepage: www.elsevier.com/locate/polymer

A sustainable bio-based benzoxazine porous organic polymer derived vanillin for synergistic catalysis: Green synthesis of Pd nanoparticles and enhanced nitro reduction

Aya Osama Mousa [a], Mohammed G. Kotp [a,b], Shiao-Wei Kuo [a,c,*]

[a] Department of Materials and Optoelectronic Science, Center for Functional Polymers and Supramolecular Materials, National Sun Yat-Sen University, Kaohsiung, 80424, Taiwan
[b] Interdisciplinary Research Center for Advanced Materials (IRC-AM), King Fahd University of Petroleum & Minerals, Dhahran, 31261, Saudi Arabia
[c] Department of Medicinal and Applied Chemistry, Kaohsiung Medical University, Kaohsiung, 807, Taiwan

ARTICLE INFO

Keywords:
Biobased benzoxazine
Porous organic polymer (POP)
Pd nanoparticles
Pollutant remediation
Environmental catalysis

ABSTRACT

A novel bio-based porous organic polymer (Gu-V-BZ POP) is successfully synthesized through Schiff base condensation using a vanillin-derived benzoxazine dialdehyde and triaminoguanidinium chloride. This approach harnesses renewable vanillin as a sustainable aromatic precursor, while the incorporated benzoxazine units enhance thermal stability and provide additional coordination sites for metal ion binding. The resulting nitrogen-rich, amine-functionalized polymer serves as an effective platform for the reduction of Pd(II) ions to well-dispersed palladium nanoparticles (Pd NPs) without the need for hazardous reducing agents. Structural and chemical characterization confirms the formation of the porous polymer network covering a surface area of 32.79 m^2 g^{-1} and the successful immobilization of ultrafine Pd NPs (~2.5 nm) on its surface. The catalytic performance of the resulting Pd@Gu-V-BZ POP nanocomposite is evaluated using the model conversion of *p*-nitrophenol (*p-NP*) to *p*-aminophenol (*p-AP*) under excess $NaBH_4$. The catalyst demonstrates exceptional activity, with apparent rate constants reaching 0.390 min^{-1} and normalized activity of 46.90 mg^{-1} s^{-1} for the composite with the highest Pd loading (0.458 wt%). Detailed kinetic analysis reveals a clear structure-activity relationship. Furthermore, comparative studies using *p*-fluoronitrobenzene suggest that the amine groups on the polymer support actively participate in substrate activation through specific interactions. This work integrates renewable feedstock chemistry, green nanoparticle synthesis, and functional benzoxazine design to create an efficient and durable catalytic material, offering a sustainable strategy for the development of high-performance heterogeneous catalysts for environmental and industrial engineering.

1. Introduction

Nitroarenes are widely disposed of from the production of dyes, pharmaceuticals, and pesticides, thus pose significant environmental and health hazards due to their high toxicity and persistence [1–9]. The reduction of nitroarenes to their corresponding aromatic amines is crucial, as amines are far less hazardous and serve as valuable intermediates in various chemical industries [10–14]. Aromatic amines (e.g. *p-aminophenol*) could be used in optoelectronic and nanocomposite [15,16]. Traditional disposal methods for nitroarenes, such as biological and chemical remediation, often result in the generation of secondary pollutants and require stringent control measures to prevent further environmental damage [17–19]. In this context, heterogeneous catalytic reduction offers a safer and more efficient approach, converting nitroarenes into amines under milder conditions with minimal environmental impact [20,21].

Palladium (Pd) nanoparticles have shown remarkable efficacy in the catalytic reduction of nitroarenes due to their superior hydrogenation capabilities [22–26]. However, a key challenge in utilizing Pd nanoparticles is their tendency to agglomerate, which can significantly reduce their catalytic performance [24,27]. To address this, a suitable support material is necessary to disperse and stabilize the nanoparticles, ensuring optimal catalytic activity [28–30]. The eco-friendly preparation of Pd nanoparticles with ethanol serving as the reducing agent

---

* Corresponding author. Department of Materials and Optoelectronic Science, Center for Functional Polymers and Supramolecular Materials, National Sun Yat-Sen University, Kaohsiung, 80424, Taiwan.

E-mail address: kuosw@faculty.nsysu.edu.tw (S.-W. Kuo).

https://doi.org/10.1016/j.polymer.2026.130126
Received 8 February 2026; Received in revised form 22 April 2026; Accepted 26 April 2026

presents a viable solution [31]. Ethanol is a non-toxic and environmentally benign solvent, making it an ideal choice for the sustainable production of Pd nanoparticles [18].

Porous organic polymers (POPs) are considered promising supports for heterogeneous catalysis given their high surface area, tuneable porosity, as well as chemical stability [25,32–38]. By integrating specific functional groups directly into their backbone, POPs can be designed to interact strongly with metal nanoparticles, preventing aggregation and enhancing catalytic activity. However, their potential as functional supports are often limited by reliance on petrochemical building blocks. Therefore, we introduce a new strategy by developing a benzoxazine-functionalized POP synthesized from sustainable precursors. For the first time, a benzoxazine-based POP is explored as a high-performance catalytic platform. Notably, benzoxazines are versatile, high-performance materials that form strong, heat-resistant, and chemically stable polymers. Their exceptional properties make them valuable across various engineering fields for creating durable, lightweight, and reliable components [39]. This novel polymer is constructed *via* simple Schiff-base condensation between triaminoguanidinium chloride (Gu-3NH$_2$) and a vanillin-derived benzoxazine dialdehyde (V-Bz-2CHO). The Gu-3NH$_2$ moiety provides a high density of nitrogen-rich and hydrogen-bonding sites, which are expected to improve metal coordination, stabilize nanoparticles, and assist in substrate activation. Meanwhile, the vanillin benzoxazine unit incorporates renewable feedstock chemistry, adds thermal stability *via* the benzoxazine ring, and supplies the aldehyde functionalities required for network formation. This synergistic design creates a support that not only firmly anchors Pd NPs but also actively participates in the catalytic cycle, offering a sustainable and efficient route for nitroarene reduction [40–43].

Vanillin-based benzoxazines are innovative materials derived from the natural compound vanillin, which is commonly extracted from vanilla beans [44,45]. These bio-based benzoxazines are synthesized through the reaction of vanillin with various amines and formaldehyde, resulting in monomers that exhibit excellent thermal stability and mechanical properties. Research has shown that vanillin-derived benzoxazines can undergo catalyst-free polymerization, making them environmentally friendly alternatives to traditional synthetic resins [46–48]. Their unique chemical structure imparts desirable characteristics such as high crosslinking density and enhanced resistance to chemicals and heat. Applications of these materials span various fields, including coatings, adhesives, and composite manufacturing, where their performance at elevated temperatures is particularly advantageous. Therefore, vanillin-based benzoxazine, derived from a renewable resource, as well contributes rigidity and sustainability to the polymer structure [49–51]. When guanidinium and vanillin are integrated into a benzoxazine framework, they are supposed to form a POP with robust structural integrity, as well as exceptional physical and chemical

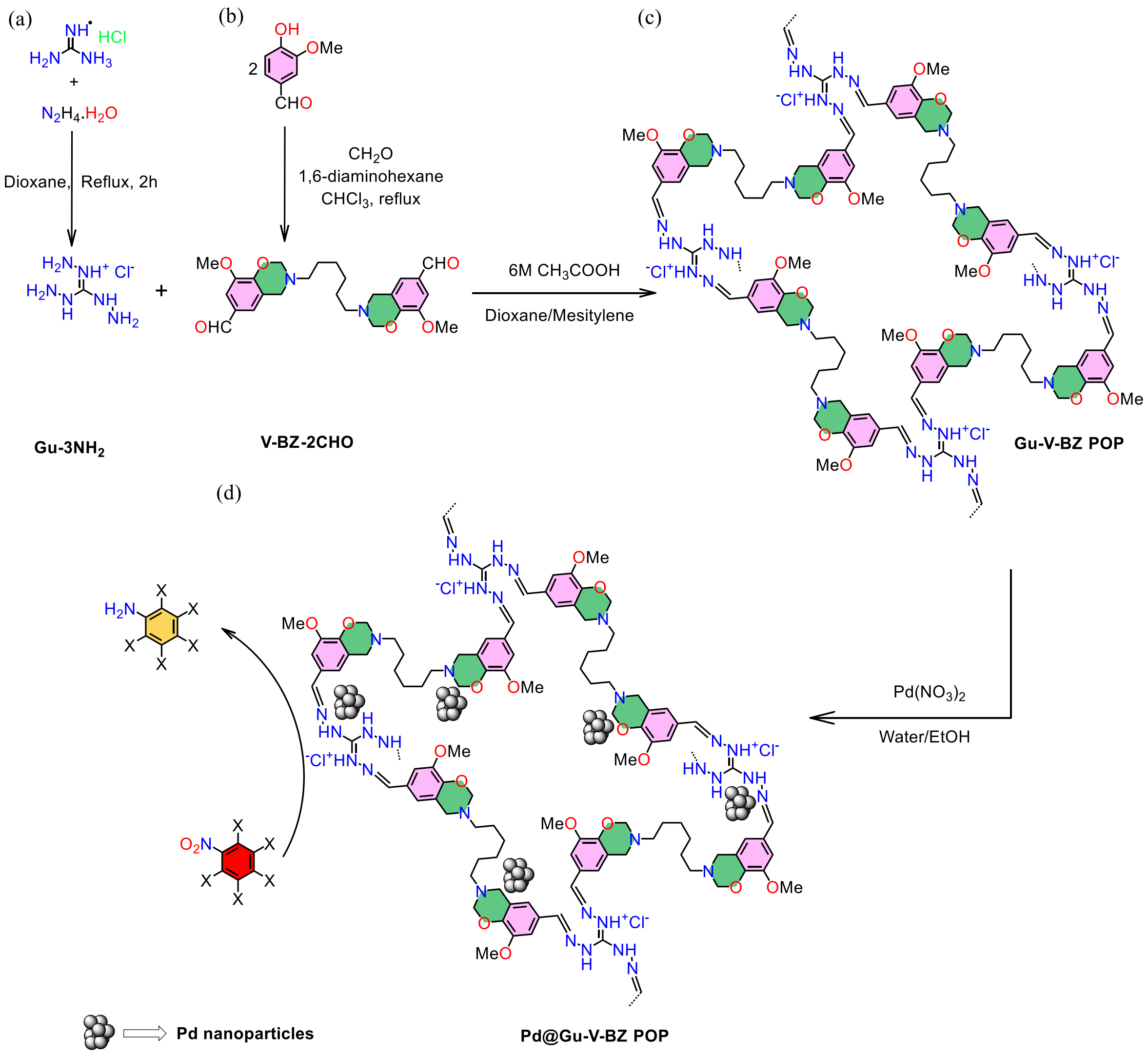

Scheme 1. Synthesis and chemical structure of (a) Gu-3NH$_2$, (b) V-BZ-2CHO, (c) Gu-V-BZ POP, and (d) Pd@Gu-V-BZ POP.

properties. We hypothesize that the unique properties of this POP make it an ideal surface for anchoring Pd nanoparticles. Moreover, the amine and oxazine groups present in our POP shall facilitate the in-situ reduction of Pd cations into Pd nanoparticles, leveraging the green reducing capabilities of the polymer matrix. This approach not only prevents the agglomeration of Pd nanoparticles but also enhances their dispersion and stability within the polymer framework. Hence, the resulting novel Pd-decorated benzoxazine POP is expected to exhibit high catalytic activity for the reduction of nitroarenes to safer aromatic amines. This green and efficient catalytic system addresses the environmental and health challenges posed by nitroarenes, providing a sustainable solution for their transformation into less hazardous compounds, as we emphasized above.

Simply, we synthesized an innovate Gu-V-BZ POP utilizing the classical Schiff base protocol between Gu-3NH$_2$ and V-BZ-2CHO (Scheme 1). The Gu-V-BZ POP showed a suitable surface area of 32.79 m^2 g^{-1} in addition to easy decoration by Pd nanoparticles. Inductively coupled plasma (ICP) spectroscopy was employed to determine the weight percentages of Pd nanoparticles (NPs) on the Gu-V-BZ POP after immersion in solutions with varying concentrations of palladium nitrate (Pd(NO$_3$)$_2$). The amino groups in the Gu-V-BZ POP nanocatalyst significantly promoted the *p*-nitrophenol (*p-NP*) reduction process *via* its phenolic hydroxyl interactions. Throughout detailed characterization and catalytic studies, we prove the synthesis of the novel biobased benzoxazine POP and their coating with Pd nanoparticles. Thereby, we demonstrate the effectiveness of this novel Pd-coated benzoxazine POP in reducing nitroarenes under environmentally friendly conditions.

2. Experimental part

2.1. Materials

Guanidine hydrochloride, 4-hydroxy-3-methoxybenzaldehyde (vanillin≥97%), and anhydrous sodium sulfate (Na$_2$SO$_4$ $\geq$ 99%) were purchased from Fluka. Palladium(II) nitrate solution (Pd(NO$_3$)$_2$ ~10 wt % in 10 wt% HNO$_3$), *p-NP* $\geq$ 99%, and sodium borohydride (NaBH$_4$ $\geq$ 98%) were sourced from Sigma-Aldrich. Hydrazine hydrate was obtained from TCI America. All other reagents-including 1,6-diaminohexane, paraformaldehyde, 1,4-dioxane, chloroform, mesitylene, tetrahydrofuran (THF), methanol, acetone, acetic acid, and ethanol-utilized just as supplied, requiring no additional purification. The trials were conducted using deionized (DI) water.

2.2. Synthesis of triaminoguanidinium chloride (Gu-3NH$_2$)

The Gu-3NH$_2$ was designed utilizing the reported methodology described by previous study [52]. Firstly, guanidine hydrochloride (1.9 g, 19.9 mmol) and hydrazine hydrate (3.4 g, 68 mmol) were mixed in 10 mL of 1,4-dioxane for 4 h in a nitrogen atmosphere, under refluxing conditions as well. The white precipitate was filtered out after the flask had cooled to ambient temperature, and enough 1,4-dioxane was then used to wash it with sufficient 1,4-dioxane to get rid of excessive hydrazine hydrate. Subsequently, the resulting white solid was vacuum-dried at 75 °C, giving 98%. Gu-3NH$_2$ characterization was corroborated by matching its FT-IR spectra with previously reported data. FTIR: 3331, 1675, 1599, and 1125 cm^{-1} (Fig. S1).

2.3. Design of aldehydic vanillin benzoxazine (V-BZ-2CHO)

The V-BZ was designed using the previous study [50]. The 4-hydroxy-3-methoxy benzaldehyde (vanillin) (6 g, 0.197 mol), 1,6-diaminohexane (2.29 g, 0.0986 mol), and paraformaldehyde (2.37 g, 0.394 mol) were introduced into a 100 mL flask, then intermixed in 70 mL of chloroform. These components were magnetically stirred under refluxing conditions overnight. The solution was separated using 0.3 M NaOH (200 mL) upon cooling the mixture. Then, the chloroform section was rinsed more three turns *via* 250 mL of water in order to neutralize the solution. Subsequently, the liquid was further dried over anhydrous Na$_2$SO$_4$ then taken out. The chloroform was separated utilizing the rotary instrument. After vacuum drying at 40 °C overnight, the white product was obtained in about 65% yield. FTIR: 3451, 2925, 3082, 1684, 1585, and 947 cm^{-1} (Fig. S2).

2.4. Design of the Gu-V-BZ POP

The Gu-V-BZ POP was designed utilizing the earlier protocol of Schiff base reaction [53], a mixture of Gu-3NH$_2$ (150 mg, 0.96 mmol), V-BZ-2CHO (0.671 mg, 1.43 mmol), acetic acid (6 M, 1.2 mL) in 1, 4-dioxane/mesitylene (5 mL/5 mL) in a Schlenk Flask (25 mL) was evacuated *via* triple turns of freeze/pump/thaw. The flask was well closed, then heated to 120 °C for three nights. Upon reaching room temperature, the brown precipitate was rinsed numerous turns respectively with THF, MeOH, and acetone. Finally, the brown solid was dried under vacuum at 70 °C overnight (87%). FTIR: 3459, 3029, 2980, 1651, 1580, and 951 cm^{-1} (Fig. 1(a)).

2.5. Design of the Pd@Gu-V-BZ POP

A double concentration of Pd(NO$_3$)$_2$ solutions -freshly prepared-solvated in ethanol/water (1:1) was made at 0.3 as well as 0.5 mmol L^{-1} concentrations. Rapidly, our Gu-V-BZ POP (100 mg) was immersed in each of the Pd(NO$_3$)$_2$ solutions (30 mL). For a full day, the mixes were magnetically agitated. Both composites were collected by centrifugation, rinsed with water, and subsequently dried at 70 °C to afford the samples *x*Pd@Gu-V-BZ POP (x = 3, 5). Pd concentrations in the 3Pd@Gu-V-BZ POP and 5Pd@Gu-V-BZ POP were 0.336 and 0.458 wt %, respectively, according to ICP spectroscopy. FTIR (powder): 3445, 2970, 3003, 1634, 1565, and 941 cm^{-1}.

2.6. Pd@Gu-V-BZ POP nanocatalyst-promoted conversion of p-NP to p-AP

A 3 mL quartz cuvette was filled with *p-NP* (2.0 mL, 0.16 mM) along with NaBH$_4$ (0.5 mL, 0.08 M), followed by 0.5 mL of *x*Pd@Gu-V-BZ POP nanocatalyst (1 mg/mL). The identical *p-NP* concentration was utilized for both samples of Pd@Gu-V-BZ POP. The responses of the reduction processes were monitored *via* a UV-Vis spectrophotometer.

2.7. Reusability of 5Pd@Gu-V-BZ POP nanocatalyst

To figure out the recovery, the nanocatalyst was multiplied sevenfold. The 5Pd@Gu-V-BZ POP nanocatalyst was utilized for five rounds; after each one, it was recovered by centrifugation and cleaned *via* water then EtOH to prevent damaging the nanocatalyst and then dried for the next cycle.

3. Results and discussion

3.1. Structural verification of monomers

The successful synthesis and structural integrity of the Gu-V-BZ POP were confirmed through a suite of spectroscopic, microscopic, and analytical techniques. Subsequently, its efficacy as a support for Pd nanoparticles and the catalytic performance of the resulting hybrid material (Pd@Gu-V-BZ) were evaluated. The molecular structures of the key precursors, triaminoguanidinium chloride (Gu-3NH$_2$) and vanillin benzoxazine dialdehyde (V-BZ-2CHO), were first verified by FTIR spectroscopy (Fig. S1 and S2). The spectrum of Gu-3NH$_2$ exhibits broad bands in the 3331–3185 cm^{-1} region, characteristic of hydrogen-bonded N–H stretching vibrations. The signature vibrational bands for the guanidinium moiety are further confirmed by peaks corresponding to N–H bending (1675 cm^{-1}), C=N stretching (1599 cm^{-1}), and C–N

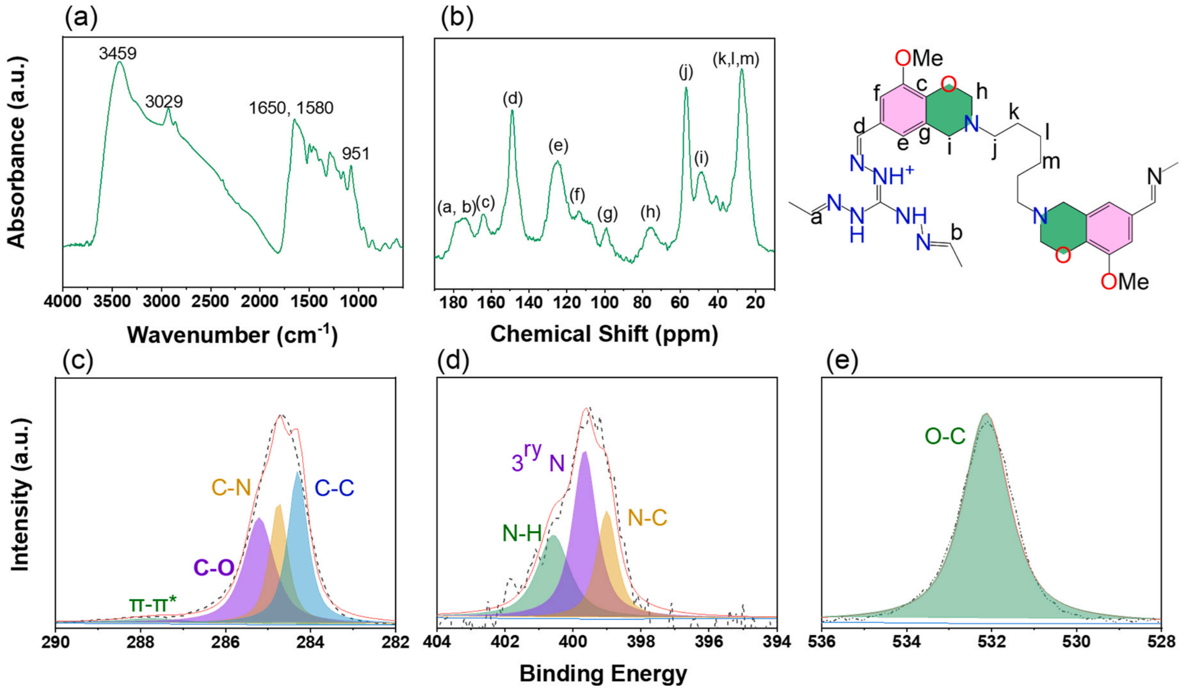

Fig. 1. (a) FTIR, (b) ^{13}C NMR, HR XPS of (c) C1s, (d) N1s, and (e) O1s of Gu-V-BZ POP.

stretching (1125 cm^{-1}) (Fig. S1) [54]. The V-BZ-2CHO monomer was synthesized according to a previously established methodology [50]. Its molecular structure was fully corroborated by complementary spectroscopic techniques. The FTIR spectrum (Fig. S2) displays characteristic vibrations at 3082 cm^{-1} (aryl C–H), 2925 cm^{-1} (aliphatic C–H), 1689 cm^{-1} (aldehyde C=O), 1585 cm^{-1} (aromatic C=C), and 947 cm^{-1} (benzoxazine ring), consistent with the target structure. Definitive confirmation was provided by ^{13}C NMR spectroscopy (Fig. S3). The spectrum exhibits all anticipated signals corresponding to the distinct carbon environments within the monomer. These include resonances for the aliphatic linker (26.04 ppm), the methylene carbons of the oxazine ring (51.00 ppm), the methoxy group (55.34 ppm), the bridging oxazine carbon (83.55 ppm), aromatic carbons (94.41–149.74 ppm), and the diagnostic aldehyde carbonyl carbon at 191.98 ppm. The thermal curing setting of the benzoxazine-containing components was investigated by differential scanning calorimetry (DSC). The DSC thermogram of the V-BZ-2CHO monomer (Fig. S4(a)) exhibits a single, sharp exothermic peak centered at 186.8 °C with the enthalpy of 344.7 J/g, matching to the benzoxazine moiety's distinctive ring-opening polymerization to create a polybenzoxazine network.

3.2. *Characterization of the Gu-V-BZ POP*

The Gu-V-BZ POP was synthesized *via* a Schiff base condensation between the aldehyde monomers of Vini-Bz-2CHO and the amine subunits of Gu-3NH$_2$. The successful formation of the imine-linked network was confirmed by FTIR spectroscopy (Fig. 1(a)). Comparative analysis of the FTIR spectra reveals definitive evidence of polymerization. The characteristic aldehyde C=O stretching band of V-BZ-2CHO at 1689 cm^{-1} and the broad N–H stretching bands of Gu-3NH$_2$ in the 3331–3185 cm^{-1} region are absent in the spectrum of the Gu-V-BZ POP. Concurrently, a new, intense band emerges at 1651 cm^{-1}, which is unequivocally referred to the C=N stretching vibration of the newly formed imine (Schiff base) linkage. Additional signals corresponding to the aromatic C=C stretch and the benzoxazine ring are observed at 951 cm^{-1}, respectively. A slight shift in these bands compared to the pristine monomers is attributed to extended conjugation within the polymer network, providing further support for successful covalent integration and POP formation.

The chemical structure of the Gu-V-BZ POP was further elucidated by ^{13}C cross-polarization magic-angle spinning (CP/MAS) solid state NMR spectroscopy (Fig. 1(b)). The spectrum provides direct evidence for the integration of both monomers into a polymeric network. The successful formation of the Schiff base linkage is conclusively confirmed by the appearance of a distinct resonance at 158 ppm, which is characteristic of an imine carbon (C=N). Simultaneously, the presence of the methoxy group from the vanillin-derived benzoxazine unit is verified by a signal at 55 ppm. The spectral region between 26.79 ppm and 176.54 ppm comprises multiple signals corresponding to the remaining aliphatic and aromatic carbon environments of the polymer framework, including the benzoxazine rings and the aromatic rings. The collective NMR data, featuring the diagnostic imine carbon signal alongside the expected framework resonances, provide definitive spectroscopic confirmation of the successful condensation reaction and the formation of the targeted Gu-V-BZ POP. X-ray photoelectron spectroscopy (XPS) was utilized to probe the surface elemental composition as well as chemical bonding states within the Gu-V-BZ POP. The survey spectrum verifies the existence of carbon, nitrogen, and oxygen as the primary constituents, with atomic percentages detailed in Fig. S3 and Table S1. High-resolution scans offer a comprehensive analysis of the chemical environment of each element. The deconvoluted C1s spectrum (Fig. 1(c)) reveals four distinct components at binding energies of 284.29, 284.74, 285.74, and 287.72 eV, assigned to sp^{2}hybridized carbon (C–C/C=C), carbon bonded to nitrogen (C–N), carbon singly bonded to oxygen (C–O), and a π-π* satellite shake-up feature, respectively [55–59]. This profile is consistent with the expected aromatic and heteroatom-rich framework of the polymer. The N1s spectrum (Fig. 1(d)) corroborates the presence of multiple nitrogen species. Deconvolution yields three peaks at 398.99, 399.64, and 400.56 eV, attributable to imine/aromatic nitrogen (C=N), tertiary amine nitrogen (3^{ry}-N), and protonated/aminated nitrogen (N–H), respectively. The coexistence of these species confirms the successful incorporation of both the guanidinium-derived and Schiff base nitrogen types into the network. Finally, the O1s spectrum (Fig. 1(e)) displays a single, symmetric peak centered at 532.12 eV, characteristic of oxygen atoms in C–O bonds, aligning with the methoxy and benzoxazine oxygen units present in the structure. Collectively, the XPS scan substantiates the surface chemical composition of the Gu-V-BZ POP and provides direct evidence for the formation of the imine linkage and the integration of the designed functional groups.

The porosity of the Gu-V-BZ POP was evaluated by N_2 physisorption at 77 K. The resulting isotherm (Fig. 2(a)) conforms to a Type II profile according to IUPAC classification, indicative of a predominantly macroporous or non-porous material with some contribution from micropores/mesopores at low relative pressures. Quantitative analysis yields a Brunauer-Emmett-Teller (BET) specific surface area of 32.79 $m^2\ g^{-1}$ and a total pore volume of 0.045 $cm^3\ g^{-1}$ (at $P/P_0 \approx 0.99$). Pore size distribution (PSD) analysis, derived from non-local density functional theory (NLDFT), reveals a multimodal structure with distinct maxima centered at 0.89, 1.54, and 3.02 nm (Fig. 2(a), onset). This PSD confirms the coexistence of micropores (<2 nm) and small mesopores within the polymer framework, aligning with the initial uptake observed in the isotherm. Although the BET surface area of the Gu-V-Bz POP is relatively modest, its high catalytic performance can be attributed to the abundance of nitrogen-rich functional groups that provide effective anchoring sites for Pd nanoparticles, enhance substrate interaction, and facilitate electron transfer during the reduction process. Moreover, the presence of ultramicroporosity and the accessibility of active sites under liquid-phase reaction conditions further support its classification as a functional POP.

The thermal robustness of the Gu-V-BZ POP was assessed by thermogravimetric analysis (TGA) under a nitrogen atmosphere (Fig. 2(b)). The polymer exhibits robust thermal endurance, with an initial decomposition temperature (corresponding to 10% weight loss, T_{d10}) of 234 °C. Furthermore, the material demonstrates a considerable char yield of 36.5 wt% upon pyrolysis at 800 °C. This significant thermal robustness and high residual mass are direct consequences of the material's crosslinked aromatic architecture. The extensive covalent network formed by Schiff base linkages and the inherent rigidity of the benzoxazine and guanidinium-derived units collectively inhibit chain mobility and volatilization, leading to enhanced decomposition resistance and efficient carbonization. The thermogram of the synthesized Gu-V-BZ POP (Fig. S4(b)) shows a single, broad exothermic peak at a significantly higher temperature of 273 °C. This pronounced shift to a higher curing temperature indicates that the benzoxazine rings within the rigid, crosslinked POP network are spatially constrained, requiring greater thermal energy to undergo the ring-opening process [60,61]. The morphology and microstructure of the Gu-V-BZ POP were explored *via* field-emission scanning electron microscopy (FE-SEM) and transmission electron microscopy (TEM). FE-SEM analysis (Fig. 2(c)) reveals that the polymer adopts a spherical particle morphology with minimal interparticle aggregation. Higher-resolution TEM imaging (Fig. 2(d)) corroborates this observation, showing discrete, well-dispersed particles with a loosely connected, open network structure. The absence of dense agglomeration and the preservation of interparticle space are consistent with the formation of a porous organic framework, facilitating mass transport and accessibility to active sites.

Elemental distribution and composition were analyzed to further characterize the Gu-V-BZ POP. Energy-dispersive X-ray spectroscopy (EDS) elemental mapping (Fig. 2(e)) verifies uniformity spatial allocation of C, N, and O throughout the polymer architecture, verifying the uniform integration of the constituent monomers. Quantitative EDS analysis (Fig. S4) provides the bulk weight percentages of these key elements as 79.10% (C), 17.53% (N), and 3.37% (O). This measured composition aligns with the theoretical stoichiometry expected for the proposed imine-linked network, offering additional validation for the successful and homogeneous formation of the target polymer.

3.3. Synthesis and characterization of Pd-loaded nanocatalysts (xPd@Gu-V-BZ POP)

Pd-decorated nanocomposites (denoted as *x*Pd@Gu-V-BZ POP, where *x* represents the nominal Pd wt%) were synthesized *via* a facile, green impregnation-reduction method. In this process, the Gu-V-BZ POP support was immersed in an ethanol solution of $Pd(NO_3)_2$. The nitrogen-rich framework, featuring amino groups from the guanidinium unit and heteroatoms within the oxazine rings, acts as an effective coordination site for Pd^{2+} ions. Subsequent in-situ reduction of the coordinated Pd(II) species to metallic Pd^0 NPs is facilitated by ethanol under mild heating, eliminating the need for external, hazardous reducing agents. Initial spectroscopic assessment of the resulting nanocomposite is provided by FTIR. The spectrum of 5Pd@Gu-V-BZ POP (Fig. 3(a)) retains all characteristic bands of the polymer support. However, a slight shift of these bands-for example, the imine C=N stretch from 1651 cm^{-1} to 1637 cm^{-1} and the benzoxazine ring signal from 950 cm^{-1} to 940 cm^{-1} is observed. These subtle shifts indicate a weak electronic interaction between the coordinated Pd species (both ions and nanoparticles) and the electron-donating nitrogen/oxygen sites of the polymer backbone, confirming successful functionalization without altering the core polymer structure [62,63].

The deposition of Pd nanoparticles significantly influenced the textural properties of the support. N_2 physisorption analysis of the 3Pd@Gu-V-BZ POP composite reveals a substantial decrease in specific surface area to 10.85 $m^2\ g^{-1}$, compared to 32.79 $m^2\ g^{-1}$ for the pristine POP (Fig. 2(a)). Concomitantly, PSD shows a narrowing, with primary maxima shifting to approximately 1.01 and 1.51 nm. This attenuation in surface area and pore volume is a direct and expected consequence of Pd incorporation. The nanoparticles occupy space either by residing within the porous framework or by adhering to the external surface, thereby

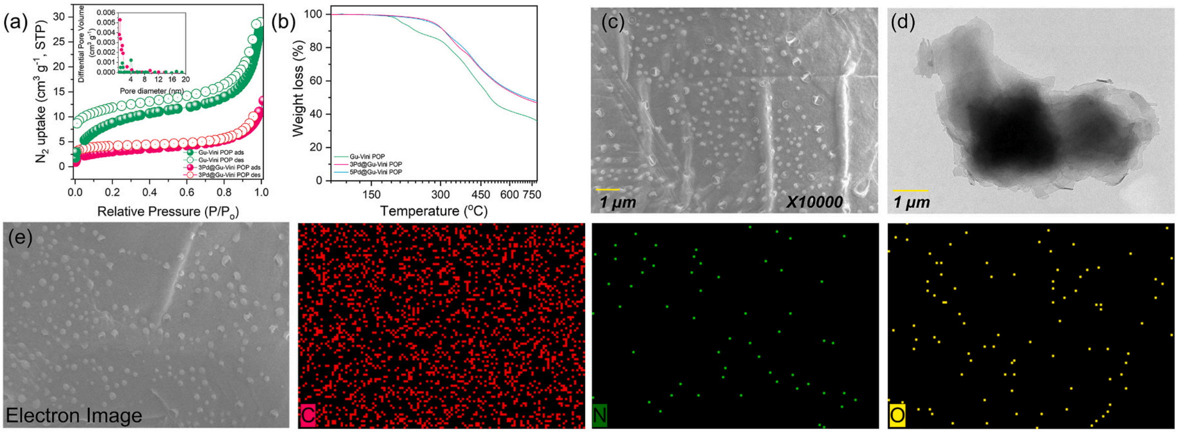

Fig. 2. (a) N_2 adsorption/desorption assays (onset: pore size distributions) and (b) TGA of Gu-V-BZ POP and Pd@Gu-V-BZ POP, (c) SEM, (d) TEM, and (e) C, N, O elemental mapping of Gu-V-BZ POP.

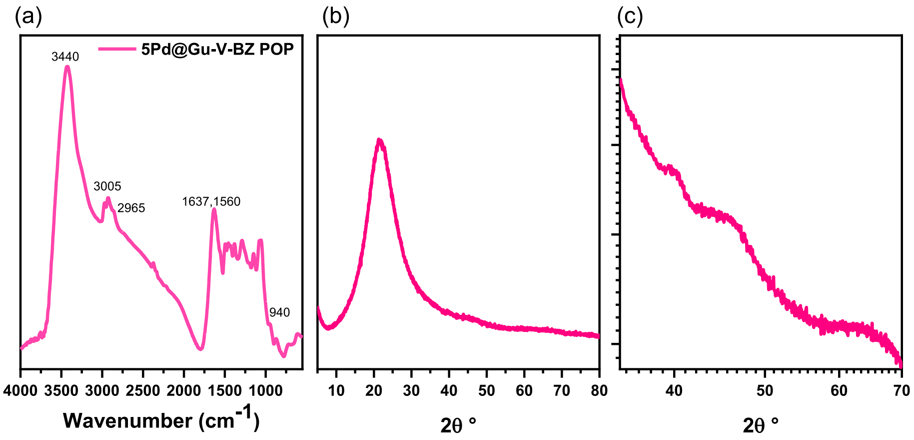

Fig. 3. (a) FTIR, (b) XRD, (c) deep XRD scan of 5Pd@Gu-V-BZ POP.

blocking N_2 adsorption sites and reducing the accessible pore volume [64]. For composites with higher Pd loadings (e.g., 5Pd@Gu-V-BZ POP), the surface area diminished below the reliable detection limit of the BET method, precluding accurate quantification. This extreme reduction further corroborates the effective and extensive decoration of the polymer support with Pd NPs. The thermal robustness of the Pd-loaded nanocomposites was considered by TGA (Fig. 2(b)). Both the 3Pd@Gu-V-BZ POP and 5Pd@Gu-V-BZ POP composites exhibit high thermal resilience, with initial decomposition temperatures (T_{d10} of 310 °C and 311 °C, respectively. Furthermore, the materials demonstrate excellent carbonization yields. The residual char yields at 800 °C under a nitrogen atmosphere are 46.8 wt% for the 3Pd composite and 47.9 wt% for the 5Pd composite. The nearly identical T_{d10} and char yield values for both composites, regardless of Pd loading, indicate that the primary thermal degradation behavior is governed by the robust, crosslinked polybenzoxazine-imine network of the Gu-V-BZ POP support. The high char yields confirm the intrinsic thermal stability and graphitization potential imparted by the aromatic benzoxazine and guanidinium-based framework. The minimal variation with Pd loading suggests that the incorporated Pd nanoparticles do not significantly alter the bulk thermal decomposition pathway of the polymer matrix, further confirming the stability of the composite structure. Upon incorporation of Pd nanoparticles, the DSC profiles of the 3Pd@Gu-V-BZ POP and 5Pd@Gu-V-BZ POP nanocomposites (Fig. S4(c)–(d)) reveal a notable change. Both composites display two distinct exothermic peaks at approximately 285.5 °C and 317.2 °C. The appearance of this doublet suggests a modification of the curing mechanism. The first peak (~285.5 °C) is likely associated with the residual benzoxazine ring-opening within the polymer framework, now slightly shifted due to interactions with the Pd nanoparticles. The second, higher-temperature peak (~317.2 °C) can be attributed to catalytic decomposition or rearrangement processes mediated by the metallic Pd nanoparticles, which can promote cleavage of chemical bonds at elevated temperatures. Therefore, the DSC analysis verifies the successful integration of thermally reactive benzoxazine monomers into the polymer matrix. The significant increase in the curing temperature from the monomer to the POP underscores the restricted mobility within the crosslinked structure. Furthermore, the altered thermal profiles of the Pd-loaded composites provide evidence of a distinct chemical interaction between the Pd nanoparticles and the benzoxazine-functionalized polymer matrix. The crystalline phase along with particle size of the supported Pd nanoparticles were investigated by X-ray diffraction (XRD) (Fig. 3(b)). The wide-angle XRD pattern of the 5Pd@Gu-V-BZ POP nanocomposite is shown in Fig. 3(b). A detailed scan (Fig. 3(c)) reveals two broad, low-intensity diffraction peaks at 2θ values of 40.1° and 46.8°. These signals correspond to the [111] and [200] lattice planes, respectively, of face-centered cubic (FCC) crystalline Pd, confirming the successful reduction of Pd^{2+} to metallic Pd(0). The broad nature of these peaks indicates the nanoscale dimensions of the Pd crystallites. The mean crystallite dimension was estimated based the full width at half maximum (FWHM) of the predominant (111) peak using the Debye-Scherrer equation of $\tau = \frac{k_{\lambda}}{\beta.\ \cos\theta}$. The calculated size is approximately 2.5 nm, which is consistent with the formation of ultrafine, well-dispersed nanoparticles on the polymer support.

XPS analysis was utilized to probe the surface oxidation states and electronic interactions within the Pd-loaded nanocomposites. High-resolution spectra for the core elements are presented in Fig. 4. The C1s, N1s, and O1s spectra of the xPd@Gu-V-BZ POP composites (Fig. 4(a)–(c)) are virtually identical to those of the pristine Gu-V-BZ POP support (Fig. 1(c)–(e)). The binding energies for the carbon (C–C, C–N, C–O), nitrogen (N–H, tertiary amine, C=N), and oxygen (C–O) components remain unchanged (see Table S1 for fitted values). This consistency confirms that the core chemical structure of the polymer support is preserved after Pd decoration and indicates a weak, non-destructive interaction between the support and the Pd nanoparticles. The critical evidence for Pd immobilization is found in the Pd 3d spectra (Fig. 4(d)). For both the 3Pd@Gu-V-BZ POP and 5Pd@Gu-V-BZ POP nanocomposites, the Pd 3d region resolves into a characteristic doublet. The primary peaks at binding energies of 334.05 eV ($3d_5/_2$) and 340.50 eV ($3d_3/_2$), with a spin-orbit splitting of 6.45 eV, are unequivocally assigned to metallic (Pd^0). The absence of significant peaks at higher binding energies (typically >335.5 eV for $3d_5/_2$) rules out the presence of substantial amounts of Pd^{2+} species, confirming the reduction of the precursor to Pd^0 nanoparticles. Furthermore, the identical Pd 3d binding energies across different loadings suggest a consistent chemical environment and electronic state for the Pd nanoparticles anchored to the support. While no pronounced Pd^{2+} peaks are observed, the presence of trace oxidized Pd species cannot be completely excluded due to possible surface oxidation.

The actual Pd loadings in the nanocomposites were quantified using ICP. The measured Pd contents for the composites derived from lower and higher precursor concentrations were 0.336 wt% and 0.458 wt%, respectively. This linear correlation between initial Pd^{2+} concentration in the impregnation solution and the final Pd content on the support demonstrates the controllability of the synthesis and the accessibility of the polymer's coordination sites for metal ion uptake.

The morphology of the nanocomposites and the dispersion of Pd nanoparticles were examined by electron microscopy. FE-SEM images (Fig. 5(a)–(b)) confirm that the spherical particle morphology of the Gu-V-BZ POP support is retained after Pd loading. High-resolution TEM analysis (Fig. 5(c)–(d)) reveals that the Pd nanoparticles are uniformly dispersed across the polymer surface without significant agglomeration, even at higher loadings. This excellent dispersion is facilitated by the combined effect of the support's accessible surface area and porous

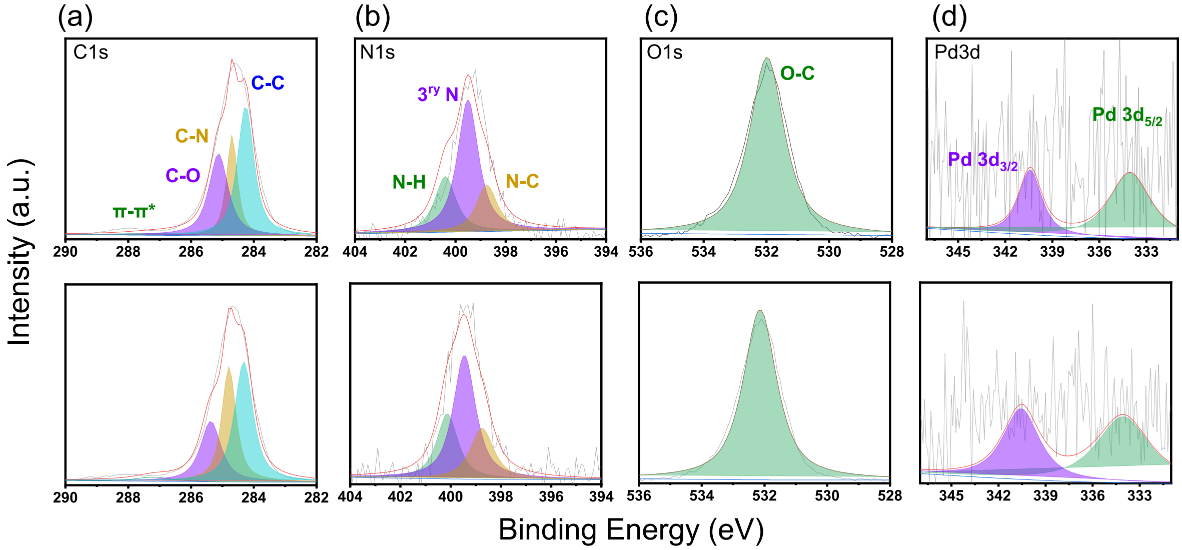

Fig. 4. HRXPS of (a) C1s, (b) N1s, (c) O1s, and (d) Pd_{3d} incorporated 3Pd@Gu-V-BZ POP.

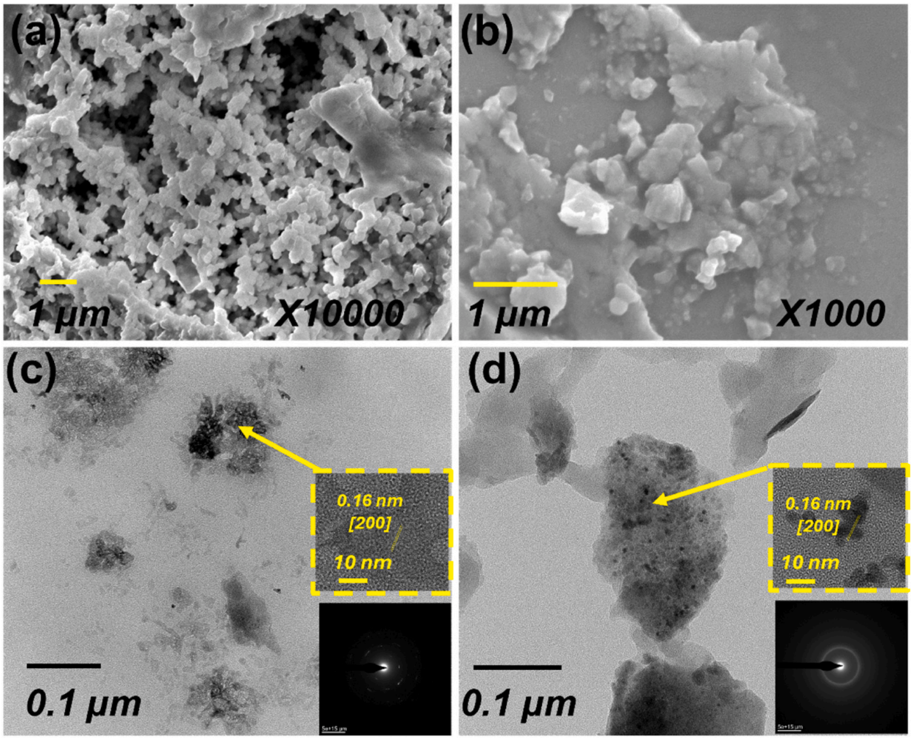

Fig. 5. (a, b) SEM, (c, d) TEM (in-situ HRTEM and SAED) of 3 and 5 Pd@Gu-V-BZ POPs.

structure, which provide ample anchoring sites. Lattice-resolved HR-TEM imaging (insets, Fig. 5(c)–(d)) provides crystallographic confirmation of the nanoparticles. The interplanar spacing of 0.16 nm lines up with the (220) lattice plane of FCC Pd. This finding is in full agreement with the XRD results (Fig. 3(c)), conclusively identifying the nanoparticles as crystalline metallic Pd.

EDS elemental mapping (Fig. 6(a) and (b) for 3Pd and 5Pd composites, respectively) demonstrates the even spread of carbon, nitrogen, and oxygen everywhere in the architecture, verifying the structural integrity of the polymer support. Crucially, the Pd signal is uniformly co-located with this framework, visually confirming the successful and even deposition of Pd nanoparticles across the support surface. The elemental composition of the Pd-loaded composites was corroborated by EDS. The measured weight percentages for 3Pd@Gu-V-BZ POP were C: 59.43%, N: 29.29%, O: 14.19%, and Pd: 0.10%; for 5Pd@Gu-V-BZ POP, the values were C: 59.64%, N: 33.86%, O: 6.30%, and Pd: 0.20% (Fig. S5). The key finding is the positive correlation in Pd content: the 5Pd composite shows approximately twice the Pd weight percentage (0.20 wt%) as the 3Pd composite (0.10 wt%). This trend aligns with and independently validates the quantitative results obtained from bulk ICP analysis, confirming the controllability of Pd loading through precursor concentration.

3.4. *Dynamic catalytic effect toward the conversion of p-NP*

The catalytic performance of the *x*Pd@Gu-V-BZ POP

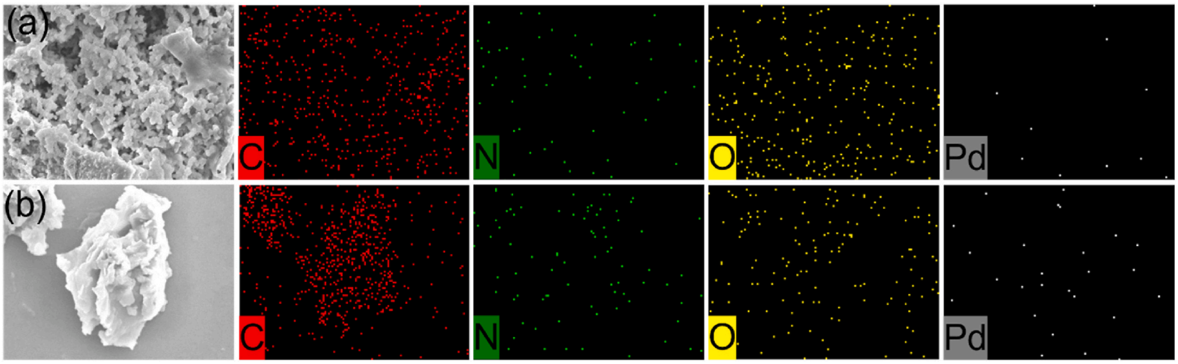

Fig. 6. Elemental mapping of C, N, O, and Pd incorporated (a) 3 and (b) 5 Pd@Gu-V-BZ POPs.

nanocomposites was evaluated using the model reduction of *p-NP* to *-p-AP* in the presence extra $NaBH_4$. This reaction is a well-established benchmark for assessing the activity of noble metal nanocatalysts in aqueous media. The reaction was monitored by UV-Vis spectroscopy. Upon addition of $NaBH_4$ to an aqueous *p-NP* solution, the absorption maximum immediately shifts from 316 nm to 400 nm, corresponding to the growth of *p*-nitrophenolate ions [10]. A control experiment using only the pristine Gu-V-BZ POP support (Fig. 7(a)) shows no significant decrease in the characteristic peak at 400 nm over time, confirming the inertness of the support and establishing that the catalytic activity originates solely from the Pd nanoparticles. In stark contrast, upon introduction of the *x*Pd@Gu-V-BZ POP nanocatalysts, the intensity of the peak at 400 nm rapidly diminishes. Concurrently, a new signal emerges at 310 nm (Fig. 7(b)–(c)), signifying the formation of the product, *p-AP*. This clear spectroscopic transformation confirms the successful and efficient catalytic function of the Pd-loaded composites. A direct comparison of catalytic activity was made by tracking the reduction kinetics catalyzed by the 3Pd@Gu-V-BZ POP and 5Pd@Gu-V-BZ POP nanocomposites. As shown in the time-dependent UV-Vis spectra (Fig. 7(b) and (c), respectively), the catalyst with the higher Pd loading exhibited significantly faster kinetics. The reaction catalyzed by 3Pd@Gu-V-BZ POP required approximately 14 min for the complete disappearance of the *p*-nitrophenolate peak at 400 nm, indicating full conversion. In contrast, the 5Pd@Gu-V-BZ POP catalyst achieved complete conversion in only about 5 min. This threefold reduction in reaction time demonstrates a clear positive correlation between Pd loading and catalytic activity, as the increased density of active Pd sites accelerates the reduction process. Further, the progress of the reaction was also evident from a distinct visual change; the deep yellow color of the *p*-nitrophenolate solution faded to colorless upon complete conversion to *p-AP*. This qualitative observation aligns perfectly with the quantitative spectroscopic data. The reaction kinetics were quantified by plotting the normalized concentration (C/C_0) of *p-NP* against time, where C_0 is the initial absorbance at 400 nm. As observed in Fig. 7(d), the C/C_0 ratio decays exponentially, confirming the gradual consumption of the reactant. The decay profile is markedly steeper for the 5Pd@Gu-V-BZ POP catalyst compared to the 3Pd@Gu-V-BZ POP, quantitatively illustrating the enhanced reaction rate achieved with higher Pd loading.

Given the large excess of $NaBH_4$ relative to *p-NP*, the reduction kinetics can be treated as pseudo-first-order with respect to *p-NP* concentration. The apparent rate constant (k_{app}) was therefore based on the linear slope of a plot of $\ln(C_0/C)$ versus time (Fig. 7(e)–(f)). The calculated (k_{app}) values were 0.222 min^{-1} and 0.390 min^{-1} for the 3Pd@Gu-V-BZ POP and 5Pd@Gu-V-BZ POP catalysts, respectively. To enable a fair comparison of intrinsic activity independent of catalyst mass, the rate constants were divided by the mass of the catalyst to account for its amount used in the reaction. The resulting mass-normalized rate constants (k_{nor}) were 26.75 mg^{-1} s^{-1} and 46.90 mg^{-1} s^{-1} for the 3Pd and 5Pd catalysts, respectively. The 1.8-fold increase in both k_{app} and k_{nor} for the 5Pd nano-catalyst directly correlates with its higher Pd loading, quantitatively confirming that the reaction rate is enhanced by increasing the density of active Pd sites on the polymer support. Realistically, the molecular size of *p-NP* (<1 nm) is compatible with the pore size distribution of the 3Pd@Gu-V-BZ POP, particularly the micropores centered at ~1.01 and 1.51 nm, which can serve as effective diffusion channels for substrate molecules to access the Pd active sites. In addition, the external surface and interparticle voids also contribute to mass transfer, especially after partial pore blocking upon Pd incorporation. Therefore, the observed catalytic performance arises from the combined effects of accessible pore channels, well-dispersed Pd nanoparticles, and strong interactions between Pd and the nitrogen-rich framework that enhance substrate adsorption and electron transfer. On the other hand, the performance of the *x*Pd@Gu-V-BZ POP nanocatalysts was benchmarked against a range of noble and non-noble metal catalysts reported for *p-NP* reduction, as compiled in Table S2. This comparison includes systems based on Pt, Cu, Ru, Ag, and Co nanoparticles supported on various matrices such as polymers, biopolymers, and composites.

A critical analysis reveals the competitive efficiency of our catalyst. When using a modest and identical dose of 0.5 mg, the 3Pd@Gu-V-BZ POP and 5Pd@Gu-V-BZ POP catalysts exhibit pseudo-first-order rate constants of $13.32 \times 10^{-3}\ s^{-1}$ and $23.4 \times 10^{-3}\ s^{-1}$, respectively. These values surpass or are competitive with those of numerous reported catalysts that often require significantly higher catalyst loadings to achieve comparable or lower rates. For instance, the k_{app} for 5Pd@Gu-V-BZ POP (0.0234 s^{-1}) is notably higher than that of Pt-decorated guar gum (0.007 s^{-1} at 5 mg) and Ru-decorated polypyrrole nanotubes (0.009 s^{-1} at 4 mg). This comparison underscores the high intrinsic activity and efficient metal utilization of the Pd nanoparticles dispersed on the Gu-V-BZ POP support. The ability to achieve a strong catalytic rate with a low catalyst mass highlights the material's practical advantage and potential for sustainable catalytic applications.

To evaluate the stability and heterogeneous nature of the catalyst, ICP analysis of the reaction filtrate was performed after completion of the reduction reaction. Only a trace amount of Pd (0.056 ppb) was detected in the solution, compared to the initial Pd concentration, indicating negligible metal leaching under the applied conditions. This result, together with the consistent catalytic performance over multiple cycles, supports the heterogeneous operation of the Pd@Gu-V-BZ POP catalyst. We note that additional tests, such as hot filtration experiments, are generally recommended to fully confirm heterogeneity and will be considered in future studies, in line with established protocols [65].

Catalytic efficiency was evaluated by calculating the turnover number (TON) as well as turnover frequency (TOF). The TON, defined as the number of moles of *p-NP* converted per mole of Pd, increased over time, reaching final values of ~49 and ~36 for the 3Pd and 5Pd catalysts, respectively (Fig. 8(a)). These values confirm that each Pd site mediates multiple catalytic cycles, demonstrating true catalytic behavior. The lower final TON for the 5Pd catalyst is a direct consequence of its higher Pd loading; the same total product is divided among

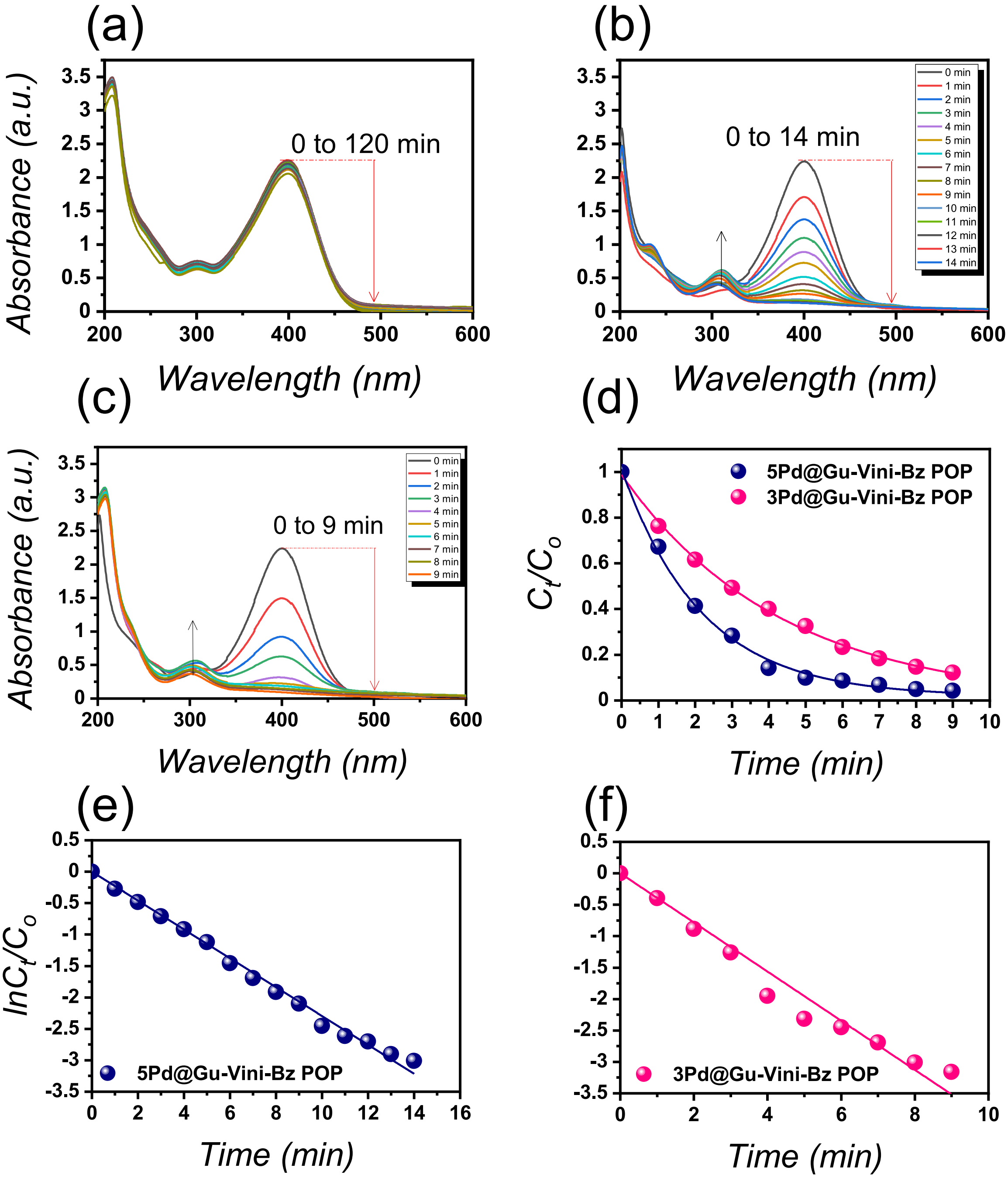

Fig. 7. UV scan profiles of the *p*-NP reduction utilizing the (a) pristine Gu-V-BZ POP, (b) 3Pd@Gu-V-BZ POP, (c) 5Pd@Gu-V-BZ POP, (d) C/C_0 curves for *x*Pd@Gu-V-BZ POP, pseudo first order kinetic model of using (e) 5Pd@Gu-V-BZ POP, and (f) 3Pd@Gu-V-BZ POP.

a greater number of active sites. The intrinsic activity per site was assessed *via* the TOF. The initial TOF (0-1 min interval) for both catalysts was nearly identical, at ~11.6 min^{-1} (Fig. 8(b)). This indicates that the fundamental activity of individual Pd sites is independent of total loading, confirming consistent nanoparticle quality and accessibility across both composites. As the reaction progressed, TOF decreased for both catalysts due to the declining concentration of *p-NP*. The TOF for the 5Pd@Gu-V-BZ POP decayed more rapidly, consistent with its faster overall substrate consumption, which leads to a steeper drop in reactant concentration. These kinetic metrics collectively demonstrate that the enhanced activity of the 5Pd@Gu-V-BZ POP nanocatalyst stems from a higher density of active sites, not from a change in their inherent catalytic quality. This structure–activity relationship-where increased loading raises the overall rate k_{app} while maintaining identical site-specific activity (TOF)-validates the successful synthesis of a tunable, well-dispersed catalytic system. To probe the role of the amine-functionalized support, the catalytic reduction was extended to substrates lacking the phenolic OH group. Under identical conditions, the reduction of *p*-fluoronitrobenzene (*p*-FNB) over the 5Pd@Gu-V-BZ POP catalyst proceeded with a normalized rate constant (k_{nor}) of 10.97 mg^{-1} s^{-1} (Fig. S6(a)–(b)). This value is approximately four times lower than that observed for *p-NP* reduction (k_{nor} = 46.90 mg^{-1} s^{-1})

The significantly attenuated rate for *p*-FNB supports the proposed mechanistic role of the support's amine groups. We posit that the phenolic OH group of *p-NP* can engage in hydrogen-bonding or acid-base interactions with the amine functionalities on the Gu-V-BZ POP.

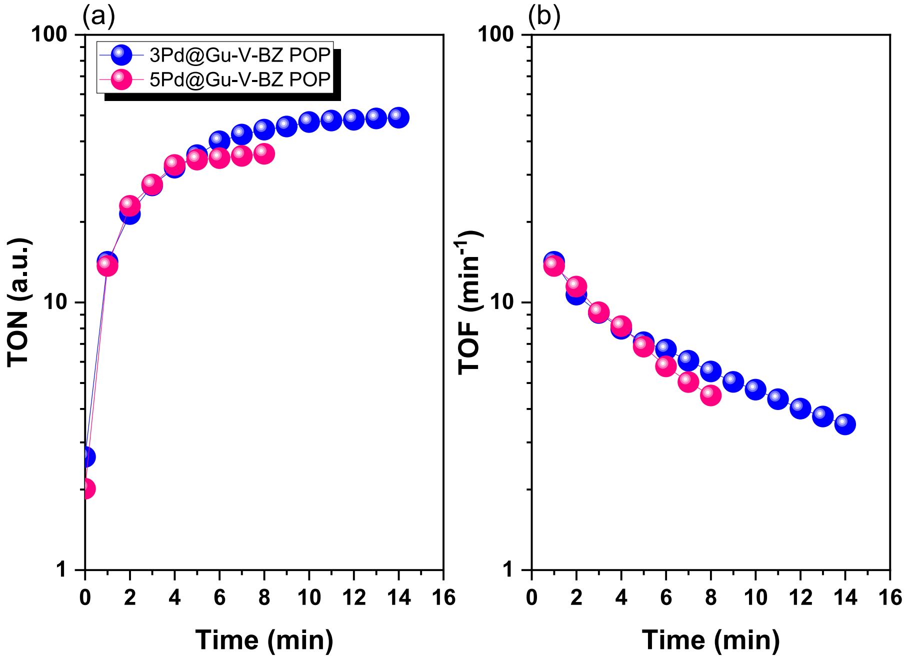

Fig. 8. (a) TONs and (b) TOFs using *x*Pd@Gu-V-BZ POP.

This favorable interaction likely facilitates the pre-concentration and optimal orientation of the *p-NP* substrate near the active Pd sites, thereby enhancing the reduction kinetics. The weaker interaction potential between the support's amines and the fluorine atom of *p*-FNB explains the observed drop in catalytic efficiency.

This hypothesis is further reinforced by the efficient conversion of *p*-nitroaniline (*p*-NA) to *p*-aminoaniline (*p*-AA), which achieved a significant k_{nor} of 10.02 $mg^{-1}\ s^{-1}$ (Fig. S6(c)–(d)). The presence of the electron-donating NH_2 group in *p*-NA, which can also interact favorably with the polymer support, contributes to its appreciable reduction rate, which lies between that of *p*-FNB and *p-NP*. Clearly, this substrate-dependent activity trend provides strong evidence that the amine-rich Gu-V-BZ POP support plays an active, cooperative role beyond merely stabilizing Pd nanoparticles. It actively participates in substrate activation *via* specific molecular interactions, leading to enhanced catalytic performance for nitroarenes with complementary functional groups.

3.5. Catalytic mechanism

The catalytic conversion of *p-NP* by $NaBH_4$ over the Pd@Gu-V-BZ POP nanocomposite is proposed to follow a surface-mediated Langmuir-Hinshelwood (L-H) mechanism, as illustrated in Scheme 2. In this model, both reactants are adsorbed onto the active Pd nanoparticle surfaces prior to reaction.

The mechanistic pathway involves several key steps. First, BH_4^- ions are chemisorbed and activated on the Pd surface. This interaction facilitates the generation of highly active hydride species (Pd–H) and the release of hydrogen. Concurrently, the *p-NP* molecule is adsorbed onto the catalyst surface. Crucially, for the 5Pd@Gu-V-BZ POP catalyst, the amine-functionalized polymer support likely promotes the adsorption and optimal orientation of *p-NP via* reactions involving its –OH group on the phenol ring, as evidenced above [66]. Once co-adsorbed in close proximity, the activated hydride species on the Pd surface transfer to the nitro group of *p-NP*. This electron/hydride transfer proceeds through a series of steps, ultimately reducing the nitro group to an amine, yielding *p-AP*, which then desorbs from the catalyst surface. The role of the Pd nanoparticles is thus twofold: (1) to activate the hydride donor (BH_4^-) and (2) to provide a conductive surface for the adsorption and subsequent electron transfer to the nitroarene substrate [67]. The amine-rich Gu-V-BZ POP support enhances this process by synergistically improving substrate affinity and concentration at the active metal sites. This cooperative effect between the metallic nanoparticles and the functional organic support underpins the high catalytic efficiency observed.

3.6. Reusability of Pd@Gu-V-BZ POP

The practical viability and potential for commercial application of a heterogeneous catalyst depend critically on its stability and reusability. The 5Pd@Gu-V-BZ POP nano-catalyst was therefore subjected to five consecutive cycles of *p-NP* reduction (Fig. 9(a)). The catalyst demonstrated excellent recyclability, retaining 85.7% of its initial reduction capacity and an apparent rate constant of 0.197 min^{-1} after the fifth run, compared to 0.390 min^{-1} for the fresh catalyst. As we mentioned above, only a trace amount of Pd (0.056 ppb) was detected in the solution based ICP, compared to the initial Pd concentration, indicating negligible metal leaching under the applied conditions. The minor attenuation in activity is attributed to a negligible physical loss of catalyst mass during the recovery and washing steps between cycles, which is common in such batch processes.

The chemical integrity of the catalyst was confirmed by FTIR spectroscopy. The spectrum of the reused 5Pd@Gu-V-BZ POP (Fig. 9(b)) is virtually identical to that of the fresh catalyst, with no observable changes in the characteristic imine (C=N), benzoxazine, or amine functional group signals. This confirms the robust chemical stability of both the Gu-V-BZ POP support and the anchored Pd nanoparticles under the reaction conditions. These findings establish the 5Pd@Gu-V-BZ POP nanocomposite as a highly efficient, stable, and reusable catalyst. More fundamentally, they validate Gu-V-BZ POP as a superior functional support, capable of firmly anchoring noble metal nanoparticles while maintaining its structural integrity, thus enabling the design of durable catalytic systems for environmental remediation. Further XPS analysis reveals that the binding energies of Pd and the main elements remain essentially unchanged compared to the fresh nanocatalyst (Fig. S8a), confirming the preservation of the chemical states and the stability of the Pd species. However, noticeable variations in surface composition were observed, including a decrease in the C1s intensity accompanied by an increase in the N1s and O1s signals. These changes are attributed to

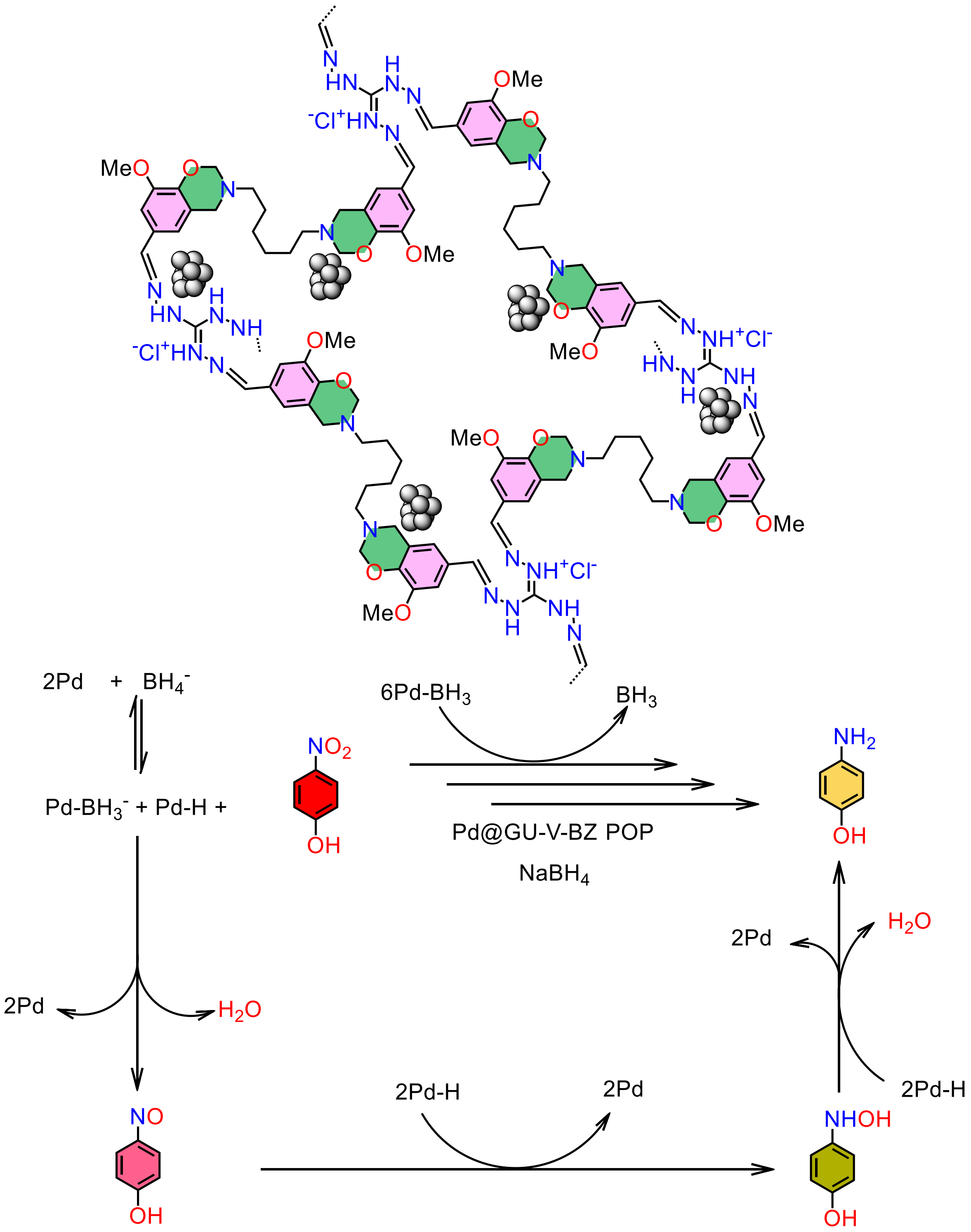

Scheme 2. Proposed catalytic reduction mechanism of *p*-nitrophenol to *p*-aminophenol by using Pd@Gu-V-BZ POP.

the adsorption of reaction products and byproducts on the catalyst surface. In particular, the enhanced N and O signals are consistent with the presence of *p*-aminophenol (–NH_2 and –OH functionalities), along with possible borate species generated from $NaBH_4$ hydrolysis. Additionally, the appearance of a feature at ~497 eV, assigned to Na KLL Auger emission, confirms the presence of residual sodium species. TEM analysis of the recycled catalyst further demonstrates that Pd nanoparticles remain uniformly dispersed on the polymer matrix (Fig. S8b), with no observable agglomeration after repeated catalytic cycles. These results collectively indicate that the catalyst retains its structural integrity, and the slight decrease in catalytic activity is primarily associated with partial surface fouling and minor physical loss during handling rather than structural degradation.

4. Conclusions

In summary, we have successfully designed and synthesized a novel amine-rich porous organic polymer, Gu-V-BZ POP, *via* a Schiff base

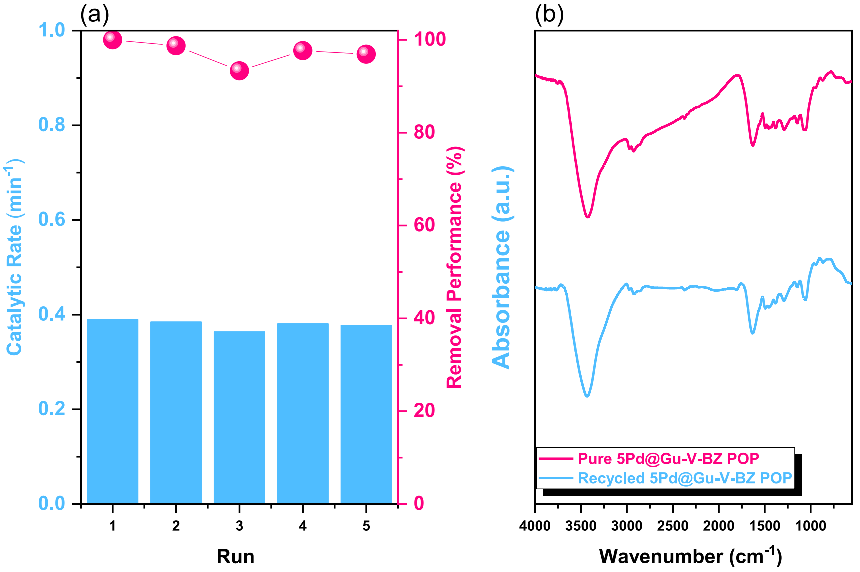

Fig. 9. (a) Catalytic Rate and Recycling performance over 5 runs and (b) FTIR before and after using 5Pd@Gu-V-BZ POP nanocatalyst.

condensation between Gu-3NH$_2$ and a V-BZ-2CHO. This functional support served as an effective platform for the in-situ synthesis and immobilization of ultrafine Pd nanoparticles (~2.5 nm) through a simple, green ethanol-mediated reduction. The resulting Pd@Gu-V-BZ POP nanocomposites demonstrated outstanding catalytic performance in the model conversion of *p-NP* to *p-AP*. Mechanistic studies revealed a synergistic role for amine-functionalized POP support. Beyond stabilizing Pd NPs, it actively participates in catalysis by promoting substrate adsorption *via* specific interactions with the reactive oxygen-hydrogen (-OH) group on *p-NP's* phenol ring, as evidenced by comparative kinetics with *p*-FNB. The catalytic process follows a surface-mediated Langmuir-Hinshelwood mechanism. Furthermore, the optimal catalyst (5Pd@Gu-V-BZ POP) exhibited excellent stability and reusability, maintaining 85.7% of its initial activity over five consecutive cycles without structural degradation. This work highlights the Gu-V-BZ POP as a versatile, functional support for crafting efficient metal nanocomposite catalysts. The strategy of integrating multiple active sites-metallic nanoparticles for activation/electron transfer and organic functional groups for substrate enrichment-provides a promising blueprint for designing advanced catalytic materials for sustainable chemical transformations and environmental remediation.

CRediT authorship contribution statement

Aya Osama Mousa: Writing – original draft, Formal analysis, Data curation, Conceptualization. **Mohammed G. Kotp:** Writing – original draft, Formal analysis, Data curation, Conceptualization. **Shiao-Wei Kuo:** Writing – review & editing, Supervision, Funding acquisition, Conceptualization.

Declaration of competing interest

The authors declare that they have no known competing financial interests or personal relationships that could have appeared to influence the work reported in this paper.

Acknowledgments

This study was financially supported by the National Science and Technology Council, Taiwan, under contracts NSTC 113-2221-E-110-012-MY3 and 114-2223-E-110-001.

Appendix. ASupplementary data

Supplementary data to this article can be found online at https://doi.org/10.1016/j.polymer.2026.130126.

Data availability

The data that has been used is confidential.

References

[1] T. Ding, S. Shu, Y. Gong, Z. Xu, W. Xu, J. Zhang, L. Shi, H. Sun, Y. Chen, B. Guo, Biomass-derived atomically dispersed Cu catalysts: synergetic roles of Cu–N$_x$ centers and hierarchically porous carbon structures in hydrogenation reduction of nitroarenes, ACS Sustain. Chem. Eng. 14 (2026) 1652–1664, https://doi.org/10.1021/acssuschemeng.5c11499.

[2] E. Arenas-Sánchez, C.E. Niño González, V. Resendiz-Bujaidar, E. Smolentseva, B. Acosta, Reduction of nitroarenes using efficient PdRu@mSiO2 nanocatalyst synthesized by a one-pot approach, Adv. Mater. Interfaces 11 (2024) 2400055, https://doi.org/10.1002/admi.202400055.

[3] P. Chaudhary, L. Ahamad, A. Chaudhary, G. Kumar, W.-J. Chen, S. Chen, Nanoparticle-mediated bioremediation as a powerful weapon in the removal of environmental pollutants, J. Environ. Chem. Eng. 11 (2023) 109591, https://doi.org/10.1016/j.jece.2023.109591.

[4] T.M. Penning, A.L. Su, K. El-Bayoumy, Nitroreduction: a critical metabolic pathway for drugs, environmental pollutants, and explosives, Chem. Res. Toxicol. 35 (2022) 1747–1765, https://doi.org/10.1021/acs.chemrestox.2c00175.

[5] C.D. Campbell, M.I. Stewart, Reflections on the teaching practices for the reduction of nitroarenes: updating methodologies and considerations of the mechanism, J. Chem. Educ. 100 (2023) 3171–3178, https://doi.org/10.1021/acs.jchemed.3c00283.

[6] X. Liu, H.Q. Li, S. Ye, Y.M. Liu, H.Y. He, Y. Cao, Gold-catalyzed direct hydrogenative coupling of nitroarenes to synthesize aromatic azo compounds, Angew. Chem. Int. Ed. 53 (2014) 7624–7628, https://doi.org/10.1002/anie.201404543.

[7] P. Cyganowski, W. Tylus, A. Dzimitrowicz, D. Jermakowicz-Bartkowiak, Design and kinetic optimization of a 3D-printed packed bed reactor for high-volume continuous hydrogenation of nitroaromatic compounds and simultaneous production of aromatic amines, Chem. Eng. J. 505 (2025) 159265, https://doi.org/10.1016/j.cej.2025.159265.

[8] S.L. Khamkar, R. Mohan, J. Santhosh, H.M. Shinde, K.L. Handore, S.V. Mohan, D. S. Reddy, Scalable and sustainable reductive amidation of nitroarenes, nitroalkenes, and nitroalkyls with acyl saccharins in aqueous media, Commun. Chem. 8 (2025) 184, https://doi.org/10.1038/s42004-025-01464-8.

[9] M. Dutta, J. Bora, T. Chetia, K. Sarmah, A.K. Guha, B. Chetia, Fabrication of CuFe2O4 decorated Ni-BTC MOF for boosting the reduction of nitroaromatic

pollutants, J. Mol. Struct. 1335 (2025) 141939, https://doi.org/10.1016/j.molstruc.2025.141939.

[10] J. Yao, D. Wang, D. Kong, M. Chu, L. Liu, F. Wang, R.P. Gaikwad, G. Zhang, S.-Q. Ni, J. Li, Spin migration-driven synergy in a Fe–Ba dual-atom catalyst for nitroaromatic reduction, ACS Catal. (2026), https://doi.org/10.1021/acscatal.5c08357.

[11] M.B. Natanzi, F. Kazemi, Z. Zand, B. Kaboudin, Highly chemoselective and fast practical visible photoreduction of nitroaromatic compounds to aromatic amines and amides using a self-assembled triad TiO2-TEOA-NC (LMCT/EDA) complex system, Green Chem. 26 (2024) 1637–1652, https://doi.org/10.1039/D3GC02563B.

[12] A. Kumar, B. Paul, R. Boukherroub, S.L. Jain, Highly efficient conversion of the nitroarenes to amines at the interface of a ternary hybrid containing silver nanoparticles doped reduced graphene oxide/graphitic carbon nitride under visible light, J. Hazard. Mater. 387 (2020) 121700, https://doi.org/10.1016/j.jhazmat.2019.121700.

[13] L. Wu, Z. Lei, M. Jia, Recent advances in selectivity control for the catalytic reduction of functionalized nitroarenes over metal-based catalysts, Dalton Trans. (2026), https://doi.org/10.1039/D5DT02581H.

[14] A.O. Mousa, M.G. Mohamed, M.G. Kotp, S.-W. Kuo, Pyrazine-tethered conjugated microporous polymers for silver nanoparticle dispersion toward enhanced catalytic reduction of p-nitrophenol and p-fluoronitrobenzene, Eur. Polym. J. 248 (2026) 114599, https://doi.org/10.1016/j.eurpolymj.2026.114599.

[15] M.G. Mohamed, W.-C. Chang, S.-W. Kuo, Crown ether- and benzoxazine-linked porous organic polymers displaying enhanced metal ion and CO2 capture through solid-state chemical transformation, Macromolecules 55 (2022) 7879–7892, https://doi.org/10.1021/acs.macromol.2c01216.

[16] W.-C. Chen, S.-W. Kuo, Ortho-imide and allyl groups effect on highly thermally stable polybenzoxazine/double-decker-shaped polyhedral silsesquioxane hybrids, Macromolecules 51 (2018) 9602–9612, https://doi.org/10.1021/acs.macromol.8b02207.

[17] M.G. Kotp, A.F.M. EL-Mahdy, T.-L. Yang, S.-W. Kuo, A pyridinyl-phenanzine conjugated microporous polymer decorated with ultrafine Ag nanoparticles mediates the rapid reduction of nitrophenol, Microporous Mesoporous Mater. 331 (2022) 111669, https://doi.org/10.1016/j.micromeso.2021.111669.

[18] M.M. Ayad, W.A. Amer, M.G. Kotp, Magnetic polyaniline-chitosan nanocomposite decorated with palladium nanoparticles for enhanced catalytic reduction of 4-nitrophenol, Mol. Catal. 439 (2017) 72–80, https://doi.org/10.1016/j.mcat.2017.06.023.

[19] M.M. Ayad, W.A. Amer, M.G. Kotp, I.M. Minisy, A.F. Rehab, D. Kopecký, P. Fitl, Synthesis of silver-anchored polyaniline-chitosan magnetic nanocomposite: a smart system for catalysis, RSC Adv. 7 (2017) 18553–18560, https://doi.org/10.1039/C7RA02575K.

[20] M. Orlandi, D. Brenna, R. Harms, S. Jost, M. Benaglia, Recent developments in the reduction of aromatic and aliphatic nitro compounds to amines, Org. Process Res. Dev. 22 (2018) 430–445, https://doi.org/10.1021/acs.oprd.6b00205.

[21] M. Nasrollahzadeh, N. Motahharifar, M. Sajjadi, A.M. Aghbolagh, M. Shokouhimehr, R.S. Varma, Recent advances in N-formylation of amines and nitroarenes using efficient (nano)catalysts in eco-friendly media, Green Chem. 21 (2019) 5144–5167, https://doi.org/10.1039/C9GC01822K.

[22] J. Sun, Y. Fu, G. He, X. Sun, X. Wang, Catalytic hydrogenation of nitrophenols and nitrotoluenes over a palladium/graphene nanocomposite, Catal. Sci. Technol. 4 (2014) 1742–1748, https://doi.org/10.1039/C4CY00048J.

[23] F.D. Sanij, P. Balakrishnan, P. Leung, A. Shah, H. Su, Q. Xu, Advanced Pd-based nanomaterials for electro-catalytic oxygen reduction in fuel cells: a review, Int. J. Hydrogen Energy 46 (2021) 14596–14627, https://doi.org/10.1016/j.ijhydene.2021.01.185.

[24] M. Iqbal, Y.V. Kaneti, J. Kim, B. Yuliarto, Y.M. Kang, Y. Bando, Y. Sugahara, Y. Yamauchi, Chemical design of palladium-based nanoarchitectures for catalytic applications, Small 15 (2019) 1804378, https://doi.org/10.1002/smll.201804378.

[25] C. Sarkar, C. Biswas, R. Paul, J. Mondal, Scientific mapping for detoxification of chemical warfare agents using porous organic polymers with internal molecular free volume, Chem. Commun. 61 (2025) 12283–12300, https://doi.org/10.1039/D5CC00963D.

[26] B. Boro, P. Koley, H.L. Tan, S. Biswas, R. Paul, S. Bhargava, W. Liu, B.M. Wong, J. Mondal, Influence of the intrinsic nanocore environment in a Pd-metalated porous organic polymer for catalytic biomass-derived furfural upgrading, ACS Appl. Nano Mater. 5 (2022) 14706–14721, https://doi.org/10.1021/acsanm.2c03052.

[27] Z. Yin, L. Lin, D. Ma, Construction of Pd-based nanocatalysts for fuel cells: opportunities and challenges, Catal. Sci. Technol. 4 (2014) 4116–4128, https://doi.org/10.1039/C4CY00760C.

[28] X. Yang, Q. Li, E. Lu, Z. Wang, X. Gong, Z. Yu, Y. Guo, L. Wang, Y. Guo, W. Zhan, Taming the stability of Pd active phases through a compartmentalizing strategy toward nanostructured catalyst supports, Nat. Commun. 10 (2019) 1611, https://doi.org/10.1038/s41467-019-09662-4.

[29] M.G. Kotp, A.M. Elewa, A.F.M. EL-Mahdy, H.-H. Chou, S.-W. Kuo, Tunable pyridyl-based conjugated microporous polymers for visible light-driven hydrogen evolution, ACS Appl. Energy Mater. 4 (2021) 13140–13151, https://doi.org/10.1021/acsaem.1c02772.

[30] T.-L. Lee, A.M. Elewa, M.G. Kotp, H.-H. Chou, A.F.M. El-Mahdy, Carbazole- and thiophene-containing conjugated microporous polymers with different planarity for enhanced photocatalytic hydrogen evolution, Chem. Commun. 57 (2021) 11968–11971, https://doi.org/10.1039/D1CC04551B.

[31] A. Trzeciak, A. Augustyniak, The role of palladium nanoparticles in catalytic C–C cross-coupling reactions, Coord. Chem. Rev. 384 (2019) 1–20, https://doi.org/10.1016/j.ccr.2019.01.008.

[32] M.G. Kotp, S.-W. Kuo, Harnessing solar energy with porous organic polymers: advancements, challenges, economic, environmental impacts and future prospects in sustainable photocatalysis, Mater. Today Chem. 41 (2024) 102299, https://doi.org/10.1016/j.mtchem.2024.102299.

[33] M.G. Kotp, M.G. Mohamed, S.-W. Kuo, Conjugated microporous polymer electrodes for supercapacitors: recent progress, key challenges, and future directions, Chem. Sci. 16 (2025) 20718–20754, https://doi.org/10.1039/D5SC05384F.

[34] M.G. Kotp, N.L. Torad, H. Nara, W. Chaikittisilp, J. You, Y. Yamauchi, A.F.M. EL-Mahdy, S.-W. Kuo, Tunable thiophene-based conjugated microporous polymers for the disposal of toxic hexavalent chromium, J. Mater. Chem. A 11 (2023) 15022–15032, https://doi.org/10.1039/D3TA00175J.

[35] M.G. Kotp, N.L. Torad, J. Lüder, A. El-Amir, W. Chaikittisilp, Y. Yamauchi, A.F.M. EL-Mahdy, A phenazine conjugated microporous polymer-based quartz crystal microbalance for sensitive detection of formaldehyde vapors at room temperature: an experiment and density functional theory study, J. Mater. Chem. A 11 (2023) 764–774, https://doi.org/10.1039/D2TA07966F.

[36] M.G. Kotp, S.-W. Kuo, Selective capturing of CO2 emissions utilizing ecological (3-mercaptopropyl)trimethoxysilane-coated porous organic polymers in composite materials, Polymers 16 (2024) 1759, https://doi.org/10.3390/polym16131759.

[37] M.G. Mohamed, A.F.M. EL-Mahdy, M.G. Kotp, S.-W. Kuo, Advances in porous organic polymers: syntheses, structures, and diverse applications, Mater. Adv. 3 (2022) 707–733, https://doi.org/10.1039/D1MA00771H.

[38] M.G. Kotp, S.-W. Kuo, Engineering porous organic polymers for enhanced CO2 capture: from synthesis to implementation, Chem. Sci. (2026), https://doi.org/10.1039/D6SC00384B.

[39] M.G. Kotp, M.G. Mohamed, A.O. Mousa, S.-W. Kuo, Rational design and molecular engineering of ultrastable porous fluorescent guanidine functionalized polybenzoxazine, Eur. Polym. J. 227 (2025) 113786, https://doi.org/10.1016/j.eurpolymj.2025.113786.

[40] J.J. Perry IV, J.A. Perman, M.J. Zaworotko, Design and synthesis of metal-organic frameworks using metal-organic polyhedra as supramolecular building blocks, Chem. Soc. Rev. 38 (2009) 1400–1417, https://doi.org/10.1039/B807086P.

[41] N. Chaoui, M. Trunk, R. Dawson, J. Schmidt, A. Thomas, Trends and challenges for microporous polymers, Chem. Soc. Rev. 46 (2017) 3302–3321, https://doi.org/10.1039/C7CS00071E.

[42] J. Xu, D. Chen, Z. Ye, S. Ma, Y. Wang, J. Zhang, Construction of a triaminoguanidine- and imidazolium-bifunctionalized ionic porous organic polymer gel as a metal-free heterogeneous catalyst for N-formylation of amines and amides with CO2 under ambient conditions, J. Catal. (2025) 116512, https://doi.org/10.1016/j.jcat.2025.116512.

[43] B. Tharmalingam, R.K. Kumar, O. Anitha, W. Kaminsky, J.G. Malecki, B. Murugesapandian, Tetra-coordinated organoboron complexes with triaminoguanidine-salicylidene based ligands: aggregation induced enhanced emission and mechanoresponsive features, Dalton Trans. 54 (2025) 3897–3910, https://doi.org/10.1039/D4DT03217A.

[44] A. Faran, A. Shomron, S.P. Singh, V. Tzin, N. Alkan, Vanillin, a fungal pathogen inhibitor: exploring its antifungal potential for postharvest applications, Postharvest Biol. Technol. 234 (2026) 114070, https://doi.org/10.1016/j.postharvbio.2025.114070.

[45] S. Kumar, F. Ullah, B. Cao, J. Ding, H.A. Keerio, S. Wang, Sustainable vanillin production: biotechnological advances, catalytic innovations, and integrated assessment, Bioresour. Technol. (2025) 133014, https://doi.org/10.1016/j.biortech.2025.133014.

[46] P. Gupta, S.K. Rastogi, B. Bhatia, S. Yadav, B. Lochab, Degradable spiroacetal-bridged bioderived polybenzoxazine thermosets, ACS Sustain. Chem. Eng. 13 (2025) 4055–4067, https://doi.org/10.1021/acssuschemeng.4c09952.

[47] A. Mariani, G. Malucelli, Biobased vitrimers: towards sustainability and circularity, Chem. Commun. 61 (2025) 2173–2189, https://doi.org/10.1039/D4CC05967K.

[48] F.I. Anagwu, V.K. Thakur, A.A. Skordos, High-performance vitrimeric benzoxazines for sustainable advanced materials: design, synthesis, and applications, Macromol. Mater. Eng. 308 (2023) 2200534, https://doi.org/10.1002/mame.202200534.

[49] M. Dai, Y. Tao, L. Fang, C. Wang, J. Sun, Q. Fang, Low dielectric polymers with high thermostability derived from biobased vanillin, ACS Sustain. Chem. Eng. 8 (2020) 15013–15019, https://doi.org/10.1021/acssuschemeng.0c05503.

[50] S. Gulyuz, B. Kiskan, Combination of polyethylenimine and vanillin-based benzoxazine as a straightforward self-healable system with excellent film-forming ability, Macromolecules 57 (2024) 2078–2089, https://doi.org/10.1021/acs.macromol.4c00005.

[51] V. Duhan, S. Yadav, C. Len, B. Lochab, Mechanochemical synthesis of environmentally benign fully biobased 4th generation benzoxazines and their polymers, Green Chem. 26 (2024) 483–497, https://doi.org/10.1039/D3GC03522K.

[52] H. Singh, M. Devi, N. Jena, M.M. Iqbal, Y. Nailwal, A. De Sarkar, S.K. Pal, Proton-triggered fluorescence switching in self-exfoliated ionic covalent organic nanosheets for selective detection of anions, ACS Appl. Mater. Interfaces 12 (2020) 13248–13255, https://doi.org/10.1021/acsami.9b20743.

[53] A.F.M. El-Mahdy, C.-H. Kuo, A. Alshehri, C. Young, Y. Yamauchi, J. Kim, S.-W. Kuo, Strategic design of triphenylamine- and triphenyltriazine-based two-dimensional covalent organic frameworks for CO2 uptake and energy storage, J. Mater. Chem. A 6 (2018) 19532–19541, https://doi.org/10.1039/C8TA04781B.

[54] S. Mitra, S. Kandambeth, B.P. Biswal, A. Khayum M, C.K. Choudhury, M. Mehta, G. Kaur, S. Banerjee, A. Prabhune, S. Verma, Self-exfoliated guanidinium-based ionic covalent organic nanosheets (iCONs), J. Am. Chem. Soc. 138 (2016) 2823–2828, https://doi.org/10.1021/jacs.5b13533.

[55] M.G. Kotp, I.M. Minisy, B. Al-Saida, S.-W. Kuo, Kinetics and selectivity insights into carbon dioxide capture utilizing carboxymethyl cellulose-polypyrrole nanocomposites: screening of silane functionalization, Carbohydr. Polym. 356 (2025) 123399, https://doi.org/10.1016/j.carbpol.2025.123399.

[56] M.G. Kotp, J. Lüder, S.-W. Kuo, A.F.M. EL-Mahdy, Phenazine-integrated conjugated microporous polymers for modulating the mechanics of supercapacitor electrodes, Mater. Adv. 5 (2024) 4142–4150, https://doi.org/10.1039/D3MA00979C.

[57] M.G. Kotp, S.-W. Kuo, A.F.M. EL-Mahdy, Phenazine-based conjugated microporous polymers: influence of planarity and imine content on energy storage performance, Colloids Surf., A 685 (2024) 133210, https://doi.org/10.1016/j.colsurfa.2024.133210.

[58] M.G. Kotp, A.F.M. El-Mahdy, M.M. Chou, S.-W. Kuo, Electronic nature of linkers based conjugated microporous polymers: a sustainable approach to enhance CO2 capture, New J. Chem. 48 (2024) 14435–14443, https://doi.org/10.1039/D4NJ02404D.

[59] M.G. Kotp, A.F.M. EL-Mahdy, S.-W. Kuo, Rational decoration of porous organic polymers with silver nanoparticles for strategic reduction of hazardous nitroaryl compounds, Polym. Chem. 16 (2025) 422–432, https://doi.org/10.1039/D4PY01179A.

[60] S. Mukherjee, B. Lochab, Hydrogen bonding-guided strategies for thermal performance modulation in biobased oxazine ring-substituted benzoxazine thermosets, Macromolecules 57 (2024) 1795–1807, https://doi.org/10.1021/acs.macromol.3c02454.

[61] R. Yang, Q. Chen, W. Sheng, K. Zhang, Oxazine ring-containing polycyclic monomers: a class of benzoxazine thermosetting resins with intrinsically low curing temperature, Macromolecules 57 (2024) 5608–5619, https://doi.org/10.1021/acs.macromol.4c00829.

[62] J. Fan, P. Wang, N. Gao, Pressure-dependent structure and electronic properties of energetic NTO crystals dominated by hydrogen-bonding interactions, Phys. Chem. Chem. Phys. 25 (2023) 14359–14367, https://doi.org/10.1039/D3CP01518A.

[63] S.H. Deshmukh, S. Yadav, T. Chowdhury, A. Pathania, S. Sapra, S. Bagchi, Probing surface interactions in CdSe quantum dots with thiocyanate ligands, Nanoscale 16 (2024) 14922–14931, https://doi.org/10.1039/D4NR01507J.

[64] L.-M. Cao, J. Zhang, X.-F. Zhang, C.-T. He, Confinement synthesis in porous molecule-based materials: a new opportunity for ultrafine nanostructures, Chem. Sci. 13 (2022) 1569–1593, https://doi.org/10.1039/D1SC05983A.

[65] N. Das, R. Paul, S. Tomar, C. Biswas, S. Chakraborty, J. Mondal, Catching an oxo vanadate porous acetylacetonate covalent adaptive catalytic network that renders mustard-gas simulant harmless, Inorg. Chem. 63 (2024) 6092–6102, https://doi.org/10.1021/acs.inorgchem.4c00519.

[66] K. Alshammari, A.S. Alakreia, G.F. Aldakhilallah, R.B. Alotaibi, M. Fal, Synthesis and characterization of CdS@g-C3N4 catalyst for enhanced hydrogen generation using methanolysis of sodium borohydride, J. Alloys Compd. 1010 (2025) 177590, https://doi.org/10.1016/j.jallcom.2024.177590.

[67] A. Chen, C. Ostrom, Palladium-based nanomaterials: synthesis and electrochemical applications, Chem. Rev. 115 (2015) 11999–12044, https://doi.org/10.1021/acs.chemrev.5b00324.